IEEE Open Journal of
Power Electronics

Received 8 July 2020; accepted 14 September 2020. Date of publication 25 September 2020;
date of current version 12 October 2020. The review of this article was arranged by Associate Editor Rafael Pena-Alzola.

Digital Object Identifier 10.1109/OJPEL.2020.3026775

An Adaptive Model Predictive Controller for Current Sensorless MPPT in PV Systems

MORCOS METRY (Member, IEEE), AND ROBERT S. BALOG (Senior Member, IEEE)

Renewable Energy and Advanced Power Electronics Research Laboratory, Department of Electrical and Computer Engineering, Texas A&M University at Qatar, Doha, QATAR

CORRESPONDING AUTHOR: MORCOS METRY (e-mail: morcos.m.metry@ieee.org).

This work was supported in part by PDRA Grant # 5-0422-19004 from the Qatar National Research Fund (a member of Qatar Foundation). The statements made herein are solely the responsibility of the authors.

ABSTRACT Finite control set model predictive control (MPC) is a model-based control method that can include multi-objective optimization, constrained control, adaptive control, and online auto-tuning of weighting factors all in a single controller that exhibits fast dynamic tracking. This paper utilizes the model-based framework of MPC to develop a sensorless current maximum power point tracking (MPPT) algorithm. Eliminating the current sensor can reduce the cost and improve the reliability of the photovoltaic system. This paper also utilizes constrained control and online auto-tuning of MPC to develop an adaptive perturbation MPPT to reduce steady-state oscillation and improve dynamic performance. This paper builds in a single framework the different layers of the MPPT problem: control, estimation, and MPPT. The proposed adaptive perturbation sensorless current mode MPPT (ASC-MPPT) technique performance is compared to the well-known incremental conductance (InCon) MPPT technique. The EN50530 European industrial test standards were used to demonstrate performance.

INDEX TERMS Photovoltaics, maximum power point tracking, model predictive control, sensorless current mode, dc/dc converters.

NOMENCLATURE

T_S	Sampling time
k	Discrete sample time step
m	The number of possible switching states
σ	Switching configuration number, $\sigma \in [1, .., m]$
n	The number of objective (cost) functions
λ	Cost function weighting factor
$g_{\sigma\in\{1:m\}}$	Cost function for state σ, where $\sigma \in [1, .., m]$
$u(k)$	Input signals in discrete-time
$y(k)$	Output variables in discrete-time
$x(k)$	State variables in discrete-time
$\tilde{x}(k)$	Estimated state variable
A	State transition matrix
B	Input matrix
C	Output matrix
i_c	Flyback converter output capacitor current
v_o	Flyback converter output voltage
R	Load resistance
C_o	Flyback converter output capacitor
i_D	Flyback converter diode current
L_m	Flyback converter magnetizing inductance
i_{Lm}	Flyback converter magnetizing inductor current
v_{Lm}	Flyback converter magnetizing inductor voltage
n	Flyback converter transformer turns ratio
v_{PV}	Photovoltaic voltage – Flyback converter input voltage
V^*_{PV}	Reference photovoltaic voltage based on the maximum power point tracking algorithm
$\tilde{v}^{\sigma}_{PV}(k+1)$	Estimated photovoltaic voltage based on flyback converter model equations at time (k+1) for state σ, where $\sigma \in [0, 1]$
$\tilde{v}_{pv,ave}$	The average predicted voltage over the period of the switching action: $\frac{1}{2}(\tilde{v}^{\sigma=0}_{PV} + \tilde{v}^{\sigma=1}_{PV})$
i_{PV}	Photovoltaic current – Flyback converter input current
$\tilde{i}_{PV}$	Estimated photovoltaic current based on the surrogate model– Estimated flyback converter input current
i_{Cin}	Flyback converter input capacitor current

C_{in}	Flyback converter input capacitor
Q_f	Flyback converter main switch
D	Flyback converter duty ratio, $D = t_{\sigma=1}/T_S$
$p - value$	The best probability of obtaining test results using Fisher's test assuming the null hypothesis is correct

I. INTRODUCTION

Solar photovoltaic energy systems (PV) have had a consistently increasing market penetration over the past seven years, with a total global installed capacity of over 500 GW [1]. A PV installation must harvest the maximum possible electrical energy at the lowest cost to be economically justifiable [2], [3]. This presents many engineering challenges and opportunities within power electronics [4] amongst which are low-cost power converter implementation [5], high reliability [6], grid-friendly integration [6], fast dynamic response to track the stochastic nature of the solar resource [7], and disturbance rejection to grid transient [8] and partial shading [9]. Maximum power point tracking (MPPT) is needed to achieve high-efficiency PV systems [10].

The MPPT subject has been well studied for PV applications, and many control algorithms are known [11]. These include perturb and observe (P&O), incremental conductance (InCon), and fractional open circuit [12]. P&O and InCon attempt to track the maximum power point (MPP) by incrementing a reference signal (voltage or current) until the system reaches the MPP [13]. These techniques may exhibit large output power oscillations around the MPP and slow settling time in response to step changes [14].

A challenge with some well-known MPPT techniques is their dependency on accurate PV current measurements [15]. Specifications for temperature drift and aging-related drift in shunt-resistor sensor and current transducer measurements can be found in the respective datasheets [16], [17]. Accuracy of the current measurement using a hall-effect sensor is influenced by the position of the conductor within the sensor [18]. Hall effect-based sensor measurements may be compromised due to magnetic core offset [19] and magnetic interference from the surrounding environment [18], [20]. Merits of other contactless current sensor technologies such as anisotropic magnetoresistive effect based sensors and tunnel magnetoresistive effect based sensors are discussed [19], [20].

Sensorless current mode control (SCM) in power converters is a way to eliminate the challenges of the current sensor [21]. An observer-based model approach to SCM as a surrogate to the current measurement is discussed [21]. Estimation of the current using capacitor voltage ripple is discussed [22]. Solutions involving the use of the transcendental relations of the PV cell to attain MPP, using a voltage sensor are demonstrated [23]. The observer-based SCM approach shows sizeable benefits on noise performance and load range [24] when compared to other known current-mode techniques [21]. Eliminating the current sensor, a fundamental component of the circuit, can reduce the cost and improves the reliability of the PV system, especially when the system involves a cascaded or a multi-level topology [25].

Finite control set model predictive control (MPC) is a model-based [26] control method that can include multi-objective optimization [27], constrained control [28], adaptive control [29] and online auto-tuning of weighting factors [30] all in a single controller that exhibits fast dynamic tracking [31]. This paper utilizes the model-based framework of MPC to develop an MPPT algorithm that eliminates the input-side current sensor in PV applications. The implementation of MPC realizes the observer-based SCM being fundamentally model-based design, expressed within the cost function. This paper also utilizes constrained control and online auto-tuning of MPC to develop an adaptive perturbation MPPT to reduce steady-state oscillation and improve dynamic performance. The contribution of this paper is proposing a single framework within MPC that performs the different layers of the MPPT problem: current model estimation, variable step-size MPPT, and converter control.

The proposed adaptive perturbation sensorless current mode MPPT (ASC-MPPT) technique performance is compared to InCon MPPT. The formulation of the proposed ASC-MPPT, applied to a flyback converter, is explained and demonstrated experimentally on a PV system using actual meteorological data. However, the technique can be applied to other converter topologies by merely modifying the MPC equations. The EN50530 European industrial test standards were used to demonstrate performance.

II. THEORETICAL FOUNDATIONS

An overview of the proposed ASC-MPPT for the flyback converter is demonstrated in Fig. 1. The flyback converter is presented in this paper for illustration as it provides electrical isolation, making it suitable for local-area dc micro-grid use [32]. Also, the low component count and low cost supplemented with a high voltage gain make it ideal for PV module-integrated topologies [33].

The controller relies on measurements of two voltage sensors: the PV input voltage (v_{PV}) and the MPPT converter output voltage (v_o), as shown in Fig. 1. Measuring the output voltage does not require additional sensors as the output voltage is already monitored in many applications, including microgrids [34], battery charge controllers [35], grid-connected inverters [36], and load monitoring [37]. Without loss of generality, the load shown in Fig. 1 is the model-based formulation of whatever is connected to the MPPT converter output [38].

The integrated MPC function estimates the PV current (i_{PV}) based on the voltage measurements. The input voltage v_{PV} at the next step is also estimated at the different states of the system (switch on and switch off). These signals are then used within the MPC cost function to determine the reference MPPT voltage and the MPPT perturbation size. The switching state that minimizes the cost function g (in Fig. 1) is applied to the flyback dc-dc converter. Without loss of generality and a slight modification in the system model, the proposed

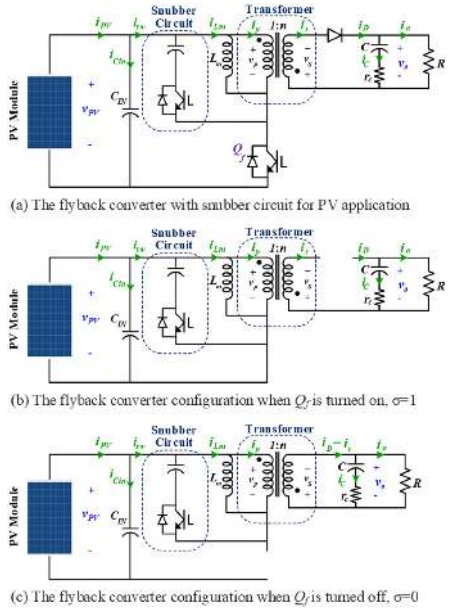

FIG. 1. The flyback converter (a) the flyback converter topology with snubber circuit for PV application. (b) The flyback converter configuration when Q_f is turned on, $\sigma = 1$. (c) The flyback converter configuration when Q_f is turned off, $\sigma = 0$.

technique could be applied to other converter topologies, and supply power to a dc-bus of an inverter or a dc microgrid.

A. REVIEW OF MPC

Finite set MPC controllers have shown potential in power electronics control applications [27]. The controller uses past and present measurements of the state variables $X(k)$, to estimate the model behavior of those state variables, $\tilde{X}(k+N)$ (the tilde denotes an estimated value and N denotes the length of the prediction horizon) [39]. This estimate, $\tilde{X}(k+N)$, is compared to a desired set reference $X^*(k+N)$ (the star denotes a reference value) to determine the control actuation vector $u(k+N)$ that minimizes a pre-defined cost function in the form:

$$g = f\left(x\left(k\right), u\left(k\right), \ldots, u\left(k+N-1\right)\right) \tag{1}$$

The control actuation vector $u(k+N)$ in power electronics is comprised of the switching state for each switching device: either 0 or 1. The time horizon is shifted by one-step, and another optimization is applied. This process is based on the moving horizon estimation principle (MHE) [39].

A cost function may have multiple objectives, and each objective could be assigned a specific weight factor, λ, depending on the application. This cost function is also bounded by the constraints of the model equations and user-defined limitations. The general form of such cost function can be formulated as

$$\begin{aligned} ming_{\sigma\in\{1:m\}} &= \lambda_1 \left|\tilde{X}_1^{\sigma}\left(k+1\right) - X_1^*\left(k+1\right)\right| \\ &\quad + \cdots + \lambda_n \left|\tilde{X}_n^{\sigma}\left(k+1\right) - X_n^*\left(k+1\right)\right| \\ \text{subject to} \quad & \tilde{x}\left(k+1\right) = Ax\left(k\right) + Bu\left(k\right) \\ & y\left(k\right) = Cx\left(k\right) \\ & \left|y\left(k\right)\right| \le y_{boundary} \end{aligned} \tag{2}$$

where σ denotes the state number in the control vector $u(k)$, m denotes the number of possible states, n denotes the number of objective functions, and λ is the weight factor for each objective.

Among the inherent challenges of finite control set MPC controllers are the variable switching frequency, which necessitates careful consideration for the sizing of passive components [40] and could cause high input current ripple [41], which adversely affects PV system performance [42]. Fixed frequency MPC addresses this issue by incorporating some elements of the PWM modulator [26], [43]–[45]. For example, [44] propose the use of triangular carriers to adjust the size of the MPC generated pulse width. The approach presented in [45] uses the converter model to estimate a discrete-time formulation for duty ratio that is dependent on system measurements and uses pulse width modulation. The approach presented in [26] and employed in this paper uses the mean value of the generated MPC signals to obtain a duty ratio to be applied to a high-frequency PWM modulator.

B. THE FLYBACK CONVERTER DISCRETE-TIME RELATIONS

Consider the flyback converter in Fig. 1. Discontinuous conduction mode (DCM) maximizes the ripple PV current; hence, the flyback converter is analyzed in continuous conduction mode (CCM). The state equations are derived based on the switching of the converter: when the switch is closed ($\sigma = 1$) and when the switch is open ($\sigma = 0$).

$$i_c^{\sigma=1}\left(t\right) = C_o\frac{dv_o}{dt} = -i_o\left(t\right) = \frac{-v_o\left(t\right)}{R} \tag{3}$$

$$i_c^{\sigma=0}\left(t\right) = C_o\frac{dv_o}{dt} = i_D - i_o = \frac{i_{Lm}\left(t\right)}{n} - \frac{v_o\left(t\right)}{R} \tag{4}$$

$$v_{Lm}^{\sigma=1}\left(t\right) = L_m\frac{di_{Lm}}{dt} = v_{PV}\left(t\right) \tag{5}$$

$$v_{Lm}^{\sigma=0}\left(t\right) = L_m\frac{di_{Lm}}{dt} = \frac{-v_o\left(t\right)}{n} \tag{6}$$

The discrete-time estimation of (3)–(6) in steady-state is found using the Euler forward method for discretization.

$$\tilde{v}_o^{\sigma=1}\left(k+1\right) = \left(1 - \frac{T_s}{RC_o}\right)v_o\left(k\right) \tag{7}$$

$$\tilde{v}_o^{\sigma=0}\left(k+1\right) = \left(1 - \frac{T_s}{RC_o}\right)v_o\left(k\right) + \frac{T_s}{nC_o}i_{Lm}\left(k\right) \tag{8}$$

$$\tilde{i}_{Lm}^{\sigma=1}\left(k+1\right) = \frac{T_s}{L_m}v_{PV}\left(k\right) + i_{Lm}\left(k\right) \tag{9}$$

$$\tilde{i}_{Lm}^{\sigma=0}\left(k+1\right) = \frac{-T_s}{nL_m}v_o\left(k\right) + i_{Lm}\left(k\right) \tag{10}$$

The magnetizing current can be expressed in terms of PV voltage and output voltage.

$$i_{Lm}^{\sigma=1}\left(t\right) = i_{PV}\left(t\right) - i_{Cin}\left(t\right) = i_{PV}\left(t\right) - C_{in}\frac{dv_{PV}}{dt} \tag{11}$$

$$i_{Lm}^{\sigma=0}(t) = n i_D(t) = n\left(i_o(t) - i_C(t)\right) = \frac{n}{R} v_o(t) - nC_o \frac{dv_o}{dt} \tag{12}$$

The discrete-time estimation of (11)–(12) in steady-state is found using the Euler backward method for discretization.

$$i_{Lm}^{\sigma=1}(k) = i_{PV}(k) - \frac{C_{in}}{T_s}\left(v_{PV}(k) - v_{PV}(k-1)\right) \tag{13}$$

$$i_{Lm}^{\sigma=0}(k) = \frac{n}{R} v_o(k) - \frac{nC_o}{T_s}\left(v_o(k) - v_o(k-1)\right) \tag{14}$$

Using equations (3) to (14) directly for MPPT implementation would require multiple sensors for the PV voltage, PV current, and the output voltage. Without loss of generality, the load R in the expressions (3)–(14) could represent a model-based expression for any load-side connected component, as discussed in [38].

C. STEADY-STATE AVERAGING

Assuming steady-state operation, the output voltage is related to the PV voltage.

$$V_o = V_{PV}\frac{nD}{1-D}, \text{ where } D = \frac{t_{\sigma=1}}{T_S} \tag{15}$$

The magnetizing current is related to the diode current by the transformer's turns ratio. Hence, the expression of average i_{LM} is

$$I_{Lm} = \frac{n\, V_o}{R(1-D)} \tag{16}$$

Relations (15) and (16) are applied to (7) and (8) to estimate the PV voltage at the next step, assuming that the PV voltage remains constant throughout the sampling period T_s.

$$\tilde{v}_{PV}^{\sigma=1}(k+1) = \left(\frac{1-D}{nD}\right)\left[1 - \frac{T_S}{RC_o}\right] v_o(k) \tag{17}$$

$$\tilde{v}_{PV}^{\sigma=0}(k+1) = \left(\frac{1-D}{nD}\right)\left[1 - \frac{T_S}{RC_o} + \frac{T_S}{RC_o(1-D)}\right] v_o(k) \tag{18}$$

The proposed ASC-MPPT algorithm uses an observer model as a surrogate for the sensor measurement of current. Hence, the surrogate model is an estimated variable in the form $\tilde{x}(k)$ and can be written as $\tilde{i}_{PV}(k)$. This estimate is used along with the measurements: $v_{PV}(k)$ and $v_o(k)$ to estimate the PV voltage state variable, $\tilde{v}_{PV}(k+1)$, at the next sampling time. The optimization process determines the appropriate actuation that will minimize the cost function in (19).

$$\begin{aligned} &min\ g_{\sigma\in\{0,1\}} = \left|\tilde{v}_{PV}^{\sigma}(k+1) - V^*_{PV}(k)\right| \\ &\text{subject to } \tilde{v}_{PV}^{\sigma=1}(k+1) = \left(\frac{1-D}{nD}\right)\left[1 - \frac{T_S}{RC_o}\right] v_o(k) \\ &\tilde{v}_{PV}^{\sigma=0}(k+1) = \left(\frac{1-D}{nD}\right)\left[1 - \frac{T_S}{RC_o} + \frac{T_S}{RC_o(1-D)}\right] v_o(k) \end{aligned} \tag{19}$$

III. PROPOSED CONTROL SCHEME

A. MPC-BASED MPPT

Previously published work on MPC-MPPT relied on a parallel InCon or P&O algorithm to determine $V^*_{PV}(k)$ in (19). Having a second loop for a parallel algorithm MPPT algorithm worsens the performance of the MPC. The contribution of this subsection is to illustrate that MPPT can be presented within the MPC framework within a single control loop. The sign of the expression $\Delta i_{PV}/\Delta v_{PV}$ is used to determine the reference value $V^*_{PV}(k)$ as is shown in (20).

$$\begin{aligned} &v^*_{PV}(k) = \begin{cases} v_{PV}(k) - |\Delta\tilde{v}|, & \mu < 0 \\ v_{PV}(k) + |\Delta\tilde{v}|, & \mu > 0 \end{cases} \\ &\text{for} \quad \mu = \frac{v_{PV}(k)\,\tilde{i}_{PV}(k) - v_{PV}(k-1)\,\tilde{i}_{PV}(k-1)}{v_{PV}(k) - v_{PV}(k-1)} \end{aligned} \tag{20}$$

where $|\Delta\tilde{v}|$ is the perturbation size of the MPPT algorithm. Based on (20) the MPPT can be expressed within the MPC cost function as illustrated in (21).

$$\begin{aligned} &ming_{\sigma\in\{0,1\}} = \left|\tilde{v}_{PV}^{\sigma}(k+1) - V^*_{PV}(k)\right| \\ &\text{subject to } \tilde{v}_{PV}^{\sigma=1}(k+1) = \left(\frac{1-D}{nD}\right)\left[1 - \frac{T_S}{RC}\right] v_o(k) \\ &\tilde{v}_{PV}^{\sigma=0}(k+1) = \left(\frac{1-D}{nD}\right)\left[1 - \frac{T_S}{RC} + \frac{T_S}{RC(1-D)}\right] v_o(k) \\ &\text{where, } V^*_{PV}(k) = \begin{cases} v_{PV}(k) - |\Delta\tilde{v}|, & \mu < 0 \\ v_{PV}(k) + |\Delta\tilde{v}|, & \mu > 0 \end{cases} \\ &\text{for} \quad \mu = \frac{v_{PV}(k)\,\tilde{i}_{PV}(k) - v_{PV}(k-1)\,\tilde{i}_{PV}(k-1)}{v_{PV}(k) - v_{PV}(k-1)} \end{aligned} \tag{21}$$

where $V^*_{PV}(k)$ is the MPPT reference. For this case, since there is only one penalty function in the MPC cost function, the weight factor $\lambda = 1$.

B. CURRENT STATE ESTIMATION

An observer model for the PV current can be obtained by analyzing the converter (Fig. 1(a)) in continuous conduction mode during the two switching states $\sigma \in \{0, 1\}$. Using Kirchhoff's current law when the primary switch is closed ($\sigma = 1$), shown in Fig. 1(b), the input capacitor current $i_{Cin}(t)$ can be written as

$$i_{Cin}(t) = i_{PV}(t) - i_{sw}(t) \tag{22}$$

As the primary switch is closed, the snubber switch is open. Hence, $i_{sw}(t) = i_{LM}(t)$. Then $i_{PV}(t)$ can be written as

$$i_{Cin}(t) = \frac{dv_{PV}(t)}{dt} = i_{PV}(t) - i_{LM}(t) \tag{23}$$

When the primary switch is open ($\sigma = 0$), the snubber switch is closed to provide a freewheeling path for the magnetizing current. Hence, $i_{sw} = 0$ and $i_{Cin}(t)$ can be written as

$$i_{Cin}(t) = \frac{dv_{PV}(t)}{dt} = i_{PV}(t) \tag{24}$$

The PV current can be written as a function of the switching state $\sigma \in \{0, 1\}$ as

$$i_{PV}(t) = \frac{d v_{PV}(t)}{dt} + \sigma i_{LM}(t) \tag{25}$$

As the change in PV current is relatively slower than the sampling time of the MPC sampling time, the expression $\sigma i_{LM}(t)$ can be approximated as

$$\sigma i_{LM}(t) \approx D I_{LM} \tag{26}$$

Substituting (16) and (26) into (25), an expression for the PV current is

$$i_{PV}(t) = \frac{nD}{(1-D)R} V_o + C_{IN} \frac{d v_{PV}(t)}{dt} \tag{27}$$

The discrete-time estimation of (27) in steady-state is found using the Euler backward method for discretization

$$\tilde{i}_{PV}(k) = \frac{nD}{(1-D)R} v_o(k) + \frac{C_{IN}}{T_S}\left(v_{PV}(k) - v_{PV}(k-1)\right) \tag{28}$$

where T_s is the sampling period of the MPC; hence, (28) is used as an observer model for PV current to eliminate the current sensor. SCM is shown to be based on the model-based design principle, which integrates within the MPC framework as in (29).

$$\begin{aligned}
&min\ g_{\sigma\in\{0,1\}} = \left|\tilde{v}^{\sigma}_{PV}(k+1) - V^{*}{}_{PV}(k)\right| \\
&\text{subject to } \tilde{v}^{\sigma=1}_{PV}(k+1) = \left(\frac{1-D}{nD}\right)\left[1 - \frac{T_S}{RC_o}\right] v_o(k) \\
&\tilde{v}^{\sigma=0}_{PV}(k+1) = \left(\frac{1-D}{nD}\right)\left[1 - \frac{T_S}{RC_o} + \frac{T_S}{RC_o(1-D)}\right] v_o(k) \\
&\tilde{i}_{PV}(k) = \frac{nD}{(1-D)R} v_o(k) + \frac{C_{IN}}{T_S}\left(v_{PV}(k) - v_{PV}(k-1)\right) \\
&\text{where, } V^{*}{}_{PV}(k) = \begin{cases} v_{PV}(k) - |\Delta\tilde{v}|, & \mu < 0 \\ v_{PV}(k) + |\Delta\tilde{v}|, & \mu > 0 \end{cases} \\
&\text{for } \mu = \frac{v_{PV}(k)\ \tilde{i}_{PV}(k) - v_{PV}(k-1)\,\tilde{i}_{PV}(k-1)}{v_{PV}(k) - v_{PV}(k-1)}
\end{aligned} \tag{29}$$

C. ADAPTIVE MPC COST FUNCTION

Predictive control based MPPT methods have shown dynamic performance improvement by reducing rising and settling times using ahead of time next step predictions. These improvements, however, were achieved using fixed step perturbation, which could be a hindrance to the performance of any MPPT method, including the predictive control-based methods. Such problems include over-stepping during steady-state, causing a high ripple, and under-stepping during a transient leading to a slower rising time. While the status of the system, transient or steady-state, is primarily dependent on ambient conditions, obtaining a measurement of irradiance is not feasible and is costly. Hence, the MPPT perturbation size estimate needs to be determined without resorting to irradiance sensors. This section demonstrates the feasibility of implementing an adaptive perturbation MPPT using the MPC cost function.

To appropriately obtain an estimate of the MPPT step size, the average PV voltage value $\tilde{v}_{pv,ave}(k+1)$, which is the average predicted voltage over the whole period of the switching action when the switch is on and when in its off, is compared with the present time PV voltage $v_{pv}(k)$. The logic here is that the difference between the predicted PV voltages at $k+1$ and the voltage at k is indicative of the step size needed to reach this predicted voltage.

$$\begin{aligned}
&|\Delta\tilde{v}| = \left|\tilde{v}_{PV,ave}(k+1) - v_{PV}(k)\right| \\
&\text{where, } \tilde{v}_{PV,ave}(k+1) = \frac{1}{2}\left(\tilde{v}^{\sigma=0}_{PV}(k+1) + \tilde{v}^{\sigma=1}_{PV}(k+1)\right)
\end{aligned} \tag{30}$$

The sign of the expression $\Delta i_{PV}/\Delta v_{PV}$ is used to determine the reference value $v^{*}_{PV,ref}(k)$ in (29), as is shown in (31).

$$\begin{aligned}
&v^{*}{}_{PV.ref}(k) = \begin{cases} v_{PV}(k) - |\Delta\tilde{v}|, & \mu < 0 \\ v_{PV}(k) + |\Delta\tilde{v}|, & \mu > 0 \end{cases} \\
&\text{for } \mu = \frac{v_{PV}(k)\ \tilde{i}_{PV}(k) - v_{PV}(k-1)\,\tilde{i}_{PV}(k-1)}{v_{PV}(k) - v_{PV}(k-1)}
\end{aligned} \tag{31}$$

Combining equations (29), (30) and (31) along with the knowledge of cost function weighting factors in MPC, as mentioned in (2), an adaptive MPC cost function is formulated in (32).

$$\begin{aligned}
g_{\sigma\in\{0,1\}} = {} & \lambda_1 \left|\tilde{v}^{\sigma}_{PV}(k+1) - v_{PV}(k) + \left|\tilde{v}_{PV,ave}(k+1) - v_{PV}(k)\right|\right| \\
& + \lambda_2 \left|\tilde{v}^{\sigma}_{PV}(k+1) - v_{PV}(k) - \left|\tilde{v}_{PV,ave}(k+1) - v_{PV}(k)\right|\right| \\
&\text{where, } \{\lambda_1, \lambda_2\} = \begin{cases} \{1, 0\}, & \mu < 0 \\ \{0, 1\}, & \mu > 0 \end{cases} \\
&\text{for } \mu = \frac{v_{PV}(k)\ \tilde{i}_{PV}(k) - v_{PV}(k-1)\,\tilde{i}_{PV}(k-1)}{v_{PV}(k) - v_{PV}(k-1)}
\end{aligned} \tag{32}$$

The overall cost function encompasses the sensorless current mode, converter discrete-time modeling, adaptive perturbation, and MPPT functionalities within one integrated objective function, as shown in (33). The detailed control implementation is detailed in the flowchart Fig. 2.

$$\begin{aligned}
&\min g_{\sigma\in\{0,1\}} \\
&= \lambda_1 \left|\tilde{v}^{\sigma}_{PV}(k+1) - v_{PV}(k) + \left|\tilde{v}_{PV,ave}(k+1) - v_{PV}(k)\right.\right. \\
&\quad \left.\left. + \lambda_2 \left|\tilde{v}^{\sigma}_{PV}(k+1) - v_{PV}(k) - \left|\tilde{v}_{PV,ave}(k+1) - v_{PV}(k)\right|\right|\right. \\
&\text{subject to } \tilde{v}^{\sigma=1}_{PV}(k+1) = \left(\frac{1-D}{nD}\right)\left[1 - \frac{T_S}{RC_o}\right] v_o(k) \\
&\tilde{v}^{\sigma=0}_{PV}(k+1) = \left(\frac{1-D}{nD}\right)\left[1 - \frac{T_S}{RC_o} + \frac{T_S}{RC_o(1-D)}\right] v_o(k) \\
&\tilde{i}_{PV}(k) = \frac{nD}{(1-D)R} v_o(k) + \frac{C_{IN}}{T_S}\left(v_{PV}(k) - v_{PV}(k-1)\right)
\end{aligned}$$

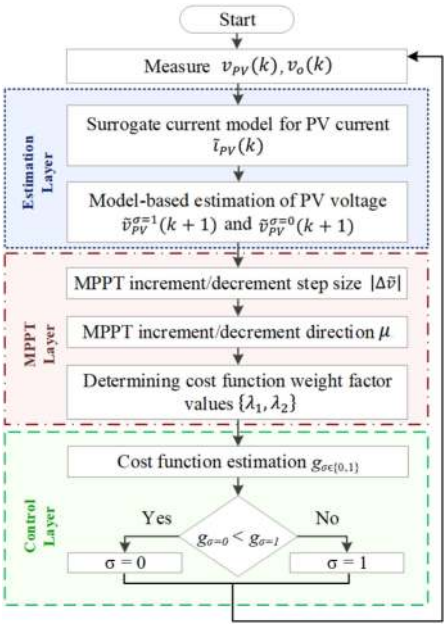

FIG. 2. A flowchart of the proposed ASC-MPPT algorithm showing the control sequence of the proposed integrated MPC cost function.

$$\text{where,} \quad \{\lambda_1, \lambda_2\} = \begin{cases} \{1, 0\}, & \mu < 0 \\ \{0, 1\}, & \mu > 0 \end{cases}$$

$$\text{for} \quad \mu = \frac{v_{PV}(k)\,\tilde{i}_{PV}(k) - v_{PV}(k-1)\,\tilde{i}_{PV}(k-1)}{v_{PV}(k) - v_{PV}(k-1)} \tag{33}$$

Fig. 2 illustrates the different layers of the proposed algorithm: estimation, control, and MPPT. Generally, MPC schemes have a prediction stage and an optimization stage. The proposed ASC-MPPT is not more complex than standard MPC controllers. The additional current estimation and the MPP reference calculation are part of the prediction stage of MPC, all encompassed in a single MPC control loop, as shown in Fig. 2.

IV. RESULTS

The PV module characteristics used in the experimental setup are given in Table I at STC (Standard Test Condition: solar irradiance = 1 kW/m^2, cell temperature = 25 °C). The PV module was modeled using two SL600-2.5 Magna-Power supplies in parallel and configured in solar array simulation (SAS) mode according to the manufacturer's recommendation. The SAS PC interface was used to implement EN50530 irradiance and temperature profiles. Sampling time of 20 μs was used in the implementation of the control algorithm on a 32-bit 200-MHz TI C2000 TMS320F28379D launchpad. Using C2000 chips for implementation provides experimental verification using an industry-standard microcontroller. The power converter hardware is a flyback converter assembled by Texas Instruments as an evaluation board for their C2000 microcontroller. The board model is TMDSSOLARUNIVKIT. To illustrate the functionality of the proposed ASC-MPPT algorithm, the built-in TI controller board TMS320F28035 was bypassed, and the flyback converter is fully controlled by the C2000 TMS320F28379D launchpad. The details of the experimental setup are as shown in Table I. A photograph of the full experimental setup used to verify the functionality of the proposed algorithm is shown in Fig. 3.

TABLE I Details of the Experimental Setup

Photovoltaic Emulator	Two parallel-connected Magna-Power SL600-2.5	
	Open-circuit voltage (V_{OC})	40 V
	Short-circuit current (I_{SC})	5.0 A
	Voltage at MPP (V_{MP}) - STC	30 V
	Current at MPP (I_{MP}) - STC	4.0 A
Controller Platform	TI C2000 TMS320F28379D for ASC-MPPT TI C2000 TMS320F28035 for InCon MPPT	
Sampling Time (T_S)	10 µs	
Load	Resistive, 500 Ohms	
Flyback Converter	TI TMDSSOLARUNIVKIT Evaluation Board	
	Output Capacitor (C)	100 µF
	Input Capacitor (C_{in})	94 µF
	Primary Switch	MOSFET, IRFB4227PBF
	Secondary Switch	Diode, CSD10060G
	Transformer	ViTEC 58PR6962
	Snubber Circuit	Active Clamp technique
	Ave. Switching Frequency	100 kHz

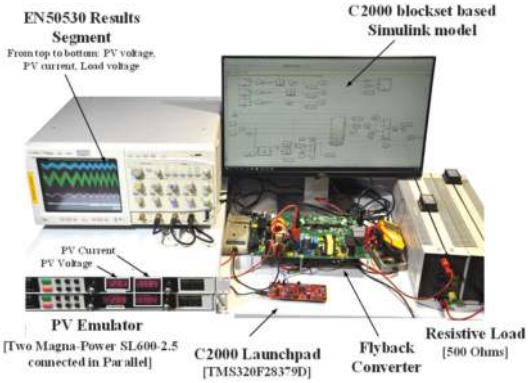

FIG. 3. A photograph of the experimental setup while running the EN50530 standardized test on the proposed ASC-MPPT algorithm.

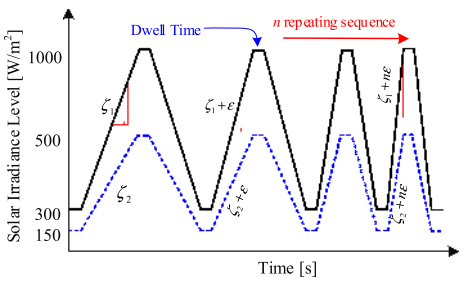

FIG. 4. The EN 50530 test sequence used in this experiment is composed of two parts: 1- Medium to high solar irradiance level (black solid line) and 2- Low to medium solar irradiance level (blue dashed line).

The dynamic EN50530 test procedure agreed upon in the European Union has gained wide acceptance as a standardized test for photovoltaic systems' MPPT accuracy and conversion efficiency [46]. The test sequence principle is demonstrated in Fig. 4. Ramp slopes ζ_n are gradually increased by a factor of

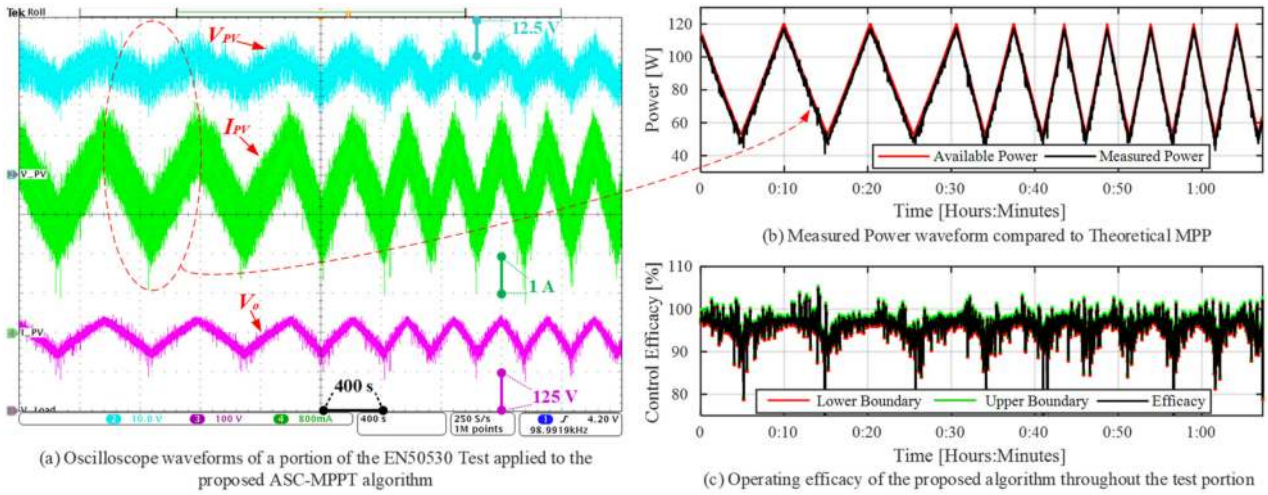

(a) Oscilloscope waveforms of a portion of the EN50530 Test applied to the proposed ASC-MPPT algorithm

(b) Measured Power waveform compared to Theoretical MPP

(c) Operating efficacy of the proposed algorithm throughout the test portion

FIG. 5. Portion of the EN 50530 standardized test applied to the experimental setup using TI C2000. (a) Oscilloscope waveforms of the experimental setup running the proposed ASC-MPPT algorithm for an hour and ten minutes long portion of the EN50530 standardized test. PV voltage, PV current and Load voltage do show the tracking throughout the timeframe of the test. (b) Actual circuit operation power waveform calculated for the experimental setup running the proposed ASC-MPPT algorithm and compared to the theoretical MPP. (c) Control efficacy of the proposed algorithm throughout the portion of the test. Upper and lower boundaries are calculated by accounting for instrumentation precision.

ε. Over the period of the test, the ramps are repeated n times. The EN 50530 irradiance profile of Fig. 4 is used to assess the performance of the flyback converter PV system controlled using the proposed ASC-MPPT algorithm.

The slopes presented in Fig. 5 are $\zeta = 3.3$ W/m^2/s and $\zeta = 6.7$ W/m^2/s, with 30 minutes for each slope. Fig. 5(a) shows oscilloscope waveforms of the experimental setup running the proposed ASC-MPPT algorithm for an hour and ten minutes long portion of the EN50530 standardized test. PV voltage, PV current, and load voltage do show the tracking throughout the timeframe of the test. The actual circuit operation power waveform calculated for the experimental setup running the proposed ASC-MPPT algorithm is shown in Fig. 5(b) and is compared to the theoretical MPP curve. The resulting control efficacy of the proposed algorithm throughout the portion of the test is shown in Fig. 5(c). Upper and lower boundaries are calculated by accounting for instrumentation precision.

V. DISCUSSION

Results shown, in general, indicate lower controller efficacy at lower insolation operation points. The total energy captured over a whole year arranged by insolation ranges is illustrated in Fig. 6. Each point on the curve represents a bin of 20 W/m^2 irradiance range. The insolation and temperature data used were based on the 2018 NREL data for the State of Arizona [47]. The captured energy in kWh is based on theoretical MPP for the setup used in this paper. The top lines show a cumulative distribution function of the percentage of energy captured over specific ranges of insolation values throughout the year. The total amount of available energy captured is 23.5% for irradiance values less than 500 W/m^2. Hence, achieving high overall system effectiveness is plausible even with more

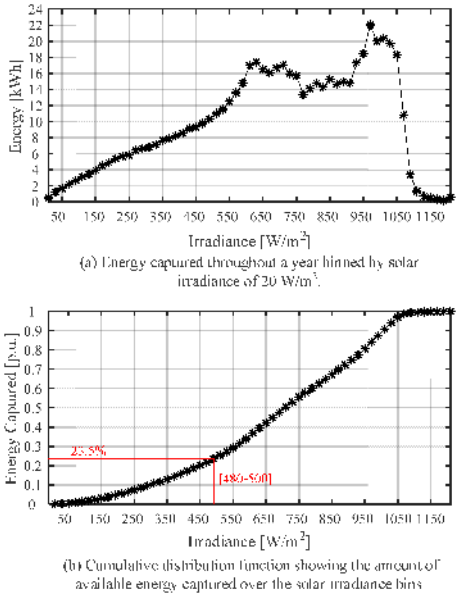

(a) Energy captured throughout a year binned by solar irradiance of 20 W/m^2.

(b) Cumulative distribution function showing the amount of available energy captured over the solar irradiance bins

FIG. 6. The insolation and temperature data used were based on the 2018 NREL data for the State of Arizona. The captured energy in kWh is based on theoretical MPP for the setup used in this paper. (a) Total energy captured throughout a year binned by solar irradiance of 20 W/m^2. (b) Cumulative distribution function showing the amount of available energy captured over the solar irradiance bins. The total amount of available energy captured is 23.5% for irradiance values less than 500 W/m^2.

reduced system performance at low insolation profiles. The rate of change per minute in the recorded NREL data varies between 0–800 W/m^2 per minute or 0–13.3 W/m^2/s. The slopes, in Fig. 5, represent over 99.8% of all the recorded transients in the NREL data.

To further understand the performance of the proposed ASC-MPPT, a 10-minute portion that is shown in Fig. 7(a)

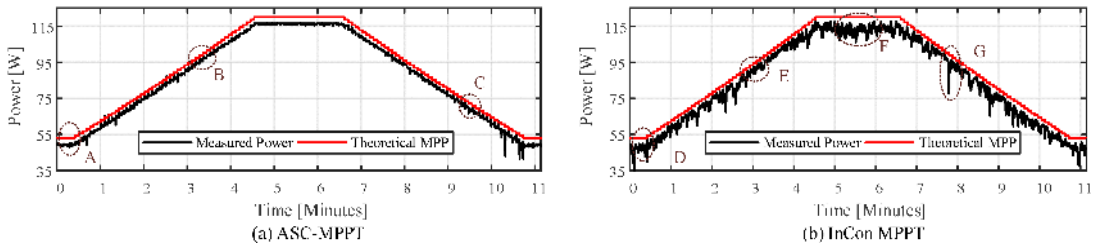

FIG. 7. An experimental comparison based on hardware tests for the proposed ASC-MPPT in comparison to Incremental Conductance (InCon) MPPT based on portion of the EN50530 testing sequence from irradiance 500 W/m² to 1000 W/m². (a) Power waveform for the experimental setup running the proposed ASC-MPPT algorithm. (b) Power waveform calculated from a ten-minute portion of the test measurements for the experimental setup running Incremental conductance MPPT. Waveform in (a) shows similar efficacy like (b), but with significantly less oscillations.

is evaluated in detail. The insolation range used is between 500 and 1000 W/m^2, which has been shown to encompass 83% of the overall energy captured (Fig. 6). A comparative study is utilized using the built-in InCon MPPT on the TI evaluation board as an illustrative reference to evaluate performance. Fig. 7(b) shows the power waveform calculated from a ten-minute portion of the test measurements for the experimental setup running InCon MPPT. Waveforms show very high oscillations around the MPP. The overall efficacy of the built-in InCon MPPT was found to be in the range of 94.8–95.6% when accounting for measurement precision. Reported fully-tuned InCon MPPT performance within the literature is shown to be in the range of 95–98% [48]. The proposed ASC-MPPT power waveforms shown in Fig. 7(c), demonstrate an overall MPPT efficacy in the range of 95.5–96.2%. These efficacy results are illustrative and could be improved by improving the fidelity of the model. The model presented in this paper solely considers first-order circuit effects. Aside from the measurement precision accounted for in calculating the efficacy range, sources of imperfection in the results include MPC model fidelity and current surrogate model parity. Without the sources of imperfection in the MPC model, the simulation results of the system were found to have a tracking efficacy of 99.4%.

Model fidelity of MPC has been studied with a detailed parameter mismatch study [49]. The study in [49] considers the effect of mismatch or deviations in load (R), output capacitor (C_o), and output capacitor ESR models from their actual values which could be caused by aging, temperature effects or load variations. Results from load mismatch show that the control efficacy of the algorithm is maintained above 99% for load size variation from −20% to 40% of the nominal load value. A two-way analysis of variances (ANOVA) study indicate that the p-value for C_o is 0.922, and the p-value of ESR is 0.0376, with an assumed p-value of 0.05 to differentiate significance. Variations of C_o from −50% to 50% of the nominal value have been found to not be significant in affecting the control efficacy. Variations in ESR from −100% to 100% of the nominal value were found to be significant. Detailed results of the parameter mismatch study and the ANOVA study are presented in [49]. The model parity of the proposed sensorless current algorithm is also studied in detail to assess the fidelity of the current observer model in comparison to the actual current sensor measurement [24]. It has been shown that an error compensation to the surrogate model can reduce the MPPT tracking error by 26.5% [24].

The results, illustrated in Fig. 7, compare the performance of the proposed algorithm with InCon MPPT. Fig. 7(a) and (b) generally show similarly effective performance results. In InCon MPPT, Fig. 7(b) detail D, the measured power exhibits high oscillations that have peaks closer to the theoretical MPP when compared to Fig. 7(a) detail A. The mean InCon MPPT efficacy at 500 W/m^2 is 90.7%, while the mean efficacy for ASC-MPPT is 88.8% at 500 W/m^2. InCon MPPT shows higher oscillation than ASC-MPPT, which is an inherent feature of any extremum seeking algorithm. Step response results from Fig. 8 show step changes of 250 W/m^2/s which is much larger than the fastest recorded transient (13.3 W/m^2/s) in the NREL data. ASC-MPPT shows better settling time in comparison to InCon MPPT in response to step changes, as is evident at the points: Fig. 8(a) detail A and Fig. 8(b) detail D. Fig. 7(b) detail F and Fig. 8(b) detail E show that InCon MPPT exhibits vigorous oscillations at 1000 W/m^2 when compared to the ASC-MPPT (Fig. 8(a) detail B). Mean efficacy of InCon MPPT at 1000 W/m^2 is 97.1%, and is 97.5% for ASC-MPPT. Fig. 7(b) detail G and Fig. 8(b) detail F also shows a very long settling time, and an undershoot in the InCon MPPT. While there is some undershoot in the ASC-MPPT, such as in Fig. 8(a) detail C, it is not as pronounced.

The impact temperature changes have on the module $P-V$ characteristics occurs over a longer time interval when compared to irradiance changes. Fig. 9 is a contour plot showing control effectiveness results for the proposed ASC-MPPT corresponding to different temperatures and insolation data as independent variables. According to Fig. 9, the proposed algorithm shows a broad region of high efficacy operating conditions when considering data in Fig. 6.

Overall the proposed ASC-MPPT has shown similar performance to InCon MPPT while achieving additional benefits. First, ASC-MPPT does not have the oscillations that are inherent to the InCon MPPT algorithm due to the adaptive perturbation feature. ASC-MPPT settles faster due to the predictive nature of MPC. The benefit of current sensorless MPPT is of particular interest in hot environments as higher temperature

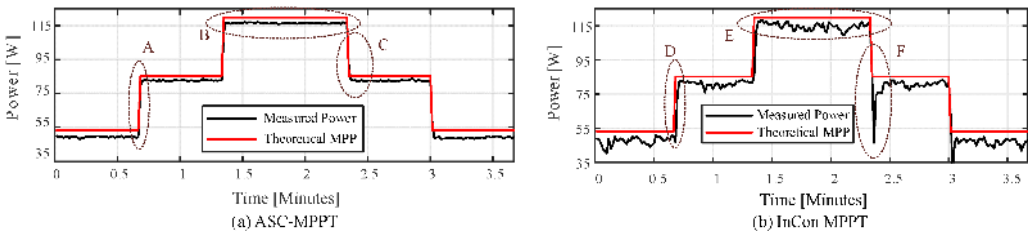

FIG. 8. An experimental comparing hardware implementation of the proposed ASC-MPPT versus InCon MPPT based on a step change test from irradiance 500 W/m^2.to 750 W/m^2 to 1000 W/m^2 and back to 750 W/m^2.then 500 W/m^2 over a period of 3.5 minutes. (a) Power waveform for the experimental setup running the proposed ASC-MPPT algorithm. (b) Power waveform calculated from a ten-minute portion of the test measurements for the experimental setup running Incremental conductance MPPT. The waveform in (a) shows lower settling time, lower steady-steady error and less oscillations than (b).

TABLE II Major Characteristics Comparison of ASC-MPPT With Other Well-Known MPPT Techniques and a Few More Advanced Algorithms

	System 1 (1 kW)	System 2 (10 kW)	System 3 (25 kW)	System 4 (100 kW)	System 5 (200 kW)
System Size	200V x 5A	500V x 20A	500V x 50A	1000V x 100A	1000V x 200A
Voltage sensor (Input+Output) [a]	$47.8 (LEM LV 25-200)	$47.8 (LEM LV 25-500)	$47.8 (LEM LV 25-500)	$47.8 (LEM LV 25-1000)	$47.8 (LEM LV 25-1000)
Current sensor [a,b]	$9.1 (LEM LES 6-NP)	$11.0 (LEM LTS 25-NP)	$15.8 (LEM LA-55P)	$22.8 (LEM LA 100 TP)	$51.8 (LEM LA-200P)
C2000 mircocontroller Chip (TMS320F28379D) [a]	$17.4	$17.4	$17.4	$17.4	$17.4
Total Cost	$122.1	$124.0	$128.8	$135.8	$156.5
% reduction in cost using sensorless current MPPT	7.5%	8.9%	12.3%	16.8%	33.1%

[a]Component pricing based on digikey.com pricing for 500 items.
[b]Closed-loop hall effect transducers considered.

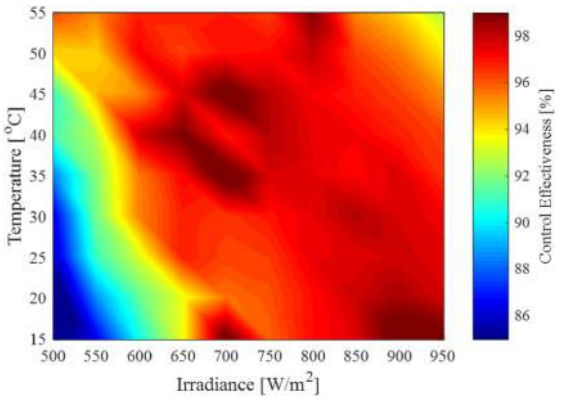

FIG. 9. A contour plot showing control effectiveness results for the proposed ASC-MPPT corresponding to different temperature and insolation data.

environments do impact the sensor measurements, temperature drift [16, 17], which reduces the efficacy and reliability of the whole system in low-power applications based on a shunt resistor and an operational amplifier for sensing. Hall-effect sensors are less prone to temperature effects, but are generally more expensive and are prone to magnetic interference, and are generally used in higher power applications [19]. Consider the comparison demonstrated in Table II of measurement and control costs for different system sizes for MPPT string and central inverter systems based on component prices from Digikey. Table III indicates that eliminating a current sensor can result in a cost reduction of up to 33% for the measurement and control of a 200 kW PV system. While the cost reduction in lower power module converters is smaller for a single module, the benefit of eliminating the current sensor becomes significant for modular systems. The significance of a current sensorless algorithm is eliminating a fundamental hardware component of the MPPT converter. Microcontrollers generally follow Moore's law and are faster to depreciate in price compared to a hall-effect current sensor. The proposed ASC-MPPT was implemented in this paper using a $17 industry-standard C2000 chip. The results can easily be performed in a $5 piccolo microcontroller with floating-point unit (FPU) and control law accelerator (CLA). Further development time for a dedicated controller, foreseeably reduces the control cost further.

ASC-MPPT is compared to some well-known techniques and other advanced methods, as presented in Table II. The comparison in Table II is one quantitative method of comparing MPPT techniques based on the reported information in the corresponding reference for illustrative purposes. The normalized convergence speed (τ_0) is based on the tracking time (τ_0) with respect to the resonance frequency of the converter, since converters are dependent on the size of the converter as presented in [55]. The proposed ASC-MPPT relies on an industrial standard C2000 microcontroller, has a single MPC control loop, has relatively fast convergence, and has high tracking efficacy in simulation.

As PV integration and PV power plants are becoming more popular, PV systems need to comply with more grid regulation standards, codes, and operational conditions [56]. Meeting

TABLE III Cost of MPPT Measurement and Control for Different Scale Converters Ranging From String to Central Inverters

Ref	MPPT Technique	PV Array Dependent?	Perturbation	Convergence Speed τ_0[a,b]	Computational Complexity[c]	Computational Loops	Sensed Parameters	Tracking Efficacy[d]
[50]	Hill-climbing/P&O	No	Fixed	1257	1 (Analog)	1 (MPPT)	2 (V, I)	97.6%
[50]	Incremental Conductance	No	Fixed	1152	2 (MSP 430 or similar)	1 (MPPT)	2 (V, I)	98.3%
[51]	Hybrid FOCV & CASM	Yes	Variable	321	3 (C2000 or similar)	1 (MPPT)	1 (V)	99.7%
[52]	Hybrid Fractional I_{SC}	Yes	Fixed	103	4 (dSPACE or similar)	1 (MPPT)	2 (V, I)	97.6%
[53]	Sliding Mode MPPT	No	Fixed	196	2 (MSP 430 or similar)	2 (Voltage, MPPT)	2 (V, I)	93.0%
[13]	Adaptive P&O	No	Variable	392	3 (C2000 or similar)	1 (MPPT)	2 (V, I)	not reported
[54]	Hybrid RCC & ESC	No	Variable	11	3 (C2000 or similar)	1 (MPPT)	2 (V, I)	99.2%
[55]	Lock-In Amplifier	No	None	20	3 (C2000 or similar)	1 (MPPT)	2 (V, I)	99.0%
Proposed Method	**ASC-MPPT**	**No**	**Variable**	**145**	**3 (C2000 or similar)**	**1 (MPC)**	**1 (V)**	**99.4%**

[a] Based on reported settling time in the simulation results in the corresponding reference, to eliminate experimental setup variations from different labs.
[b] The tracking time is normalized to the converter resonance frequency as presented in [55] $\tau_0 = \tau_0/(2\pi\sqrt{C_oL})$, where τ_0 is the settling time in seconds.
[c] Based on the reported controller used in the corresponding reference.
[d] Based on reported tracking efficacy in the simulation results of the corresponding reference.

grid standards requires special considerations in the design of PV systems as in [57]. Many times PV systems are oversized to meet load demand better and counteract the effects of low insolation, high temperature, pollution, and age degradation on the system [58]. Hence, operating at the MPP, as presented in this paper, may not be a priority during portions of the solar day. Different flexible power point techniques are employed to increase the functionality of the PV system as surveyed in [59]. The presented adaptive MPC framework can accommodate different operation modes by adjusting the cost function (33) to include more objectives such as power curtailment and low voltage ride-through.

VI. CONCLUSION

This paper presented an adaptive MPC cost function that uses the characteristics of MPC to implement an adaptive perturbation, sensorless current MPPT algorithm. Various aspects of the adaptive sensorless current MPC controller have been published separately; this paper presents a conclusive framework. The European standardized test EN50530 was used to evaluate the performance of the proposed MPPT technique. Experimental results and a comparative study to incremental conductance were presented.

ACKNOWLEDGMENT

The author thanks Dr. Wesam Rohouma and Dr. Naki Guler for their valuable insights on this article.

REFERENCES

[1] IEA International Energy Agency. PVPS 2019: Snapshot of Global PV Markets. 2019. [Online]. Available: www.iea-pvps.org
[2] R. Fu, D. Feldman, and R. Margolis, "*U.S. Solar Photovoltaic System Cost Benchmark: Q1 2018*," National Renewable Energy Laboratory, Golden, CONREL/TP-6A20-72399, Nov. 2018, Available: https://www.nrel.gov/docs/fy19osti/72399.pdf
[3] K. A. W. Horowitz, T. Remo, B. Smith, and A. Prtak, "*A Techno-Economic Analysis and Cost Reduction Roadmap for III-V Solar Cells*," National Renewable Energy Laboratory, Golden, CONREL/TP-6A20-72103, Nov. 2018, [Online]. Available: https://www.nrel.gov/docs/fy19osti/72103.pdf
[4] Y. Yang, K. A. Kim, F. Blaabjerg, and A. Sangwongwanich, *Advances in Grid-Connected Photovoltaic Power Conversion Systems*. Sawston, Cambridge, U.K.: Woodhead Publishing, 2018.
[5] O. Lopez-Lapena, "Time-division multiplexing control of multi-input converters for low-power solar energy harvesters," *IEEE Trans. Ind. Electron.*, vol. 65, no. 12, pp. 9668–9676, Dec. 2018.
[6] F. Blaabjerg, Y. Yang, D. Yang, and X. Wang, "Distributed power-generation systems and protection," *Proc. IEEE*, vol. 105, no. 7, pp. 1311–1331, Jul. 2017.
[7] T. Ding, Q. Yang, Y. Yang, C. Li, Z. Bie, and F. Blaabjerg, "A data-driven stochastic reactive power optimization considering uncertainties in active distribution networks and decomposition method," *IEEE Trans. Smart Grid*, vol. 9, no. 5, pp. 4994–5004, Sep. 2018.
[8] R. Errouissi and A. Al-Durra, "Disturbance-observer-based control for dual-stage grid-tied photovoltaic system under unbalanced grid voltages," *IEEE Trans. Ind. Electron.*, vol. 66, no. 11, pp. 8925–8936, Nov. 2019.
[9] S. Qin, C. B. Barth, and R. C. N. Pilawa-Podgurski, "Enhancing microinverter energy capture with submodule differential power processing," *IEEE Trans. Power Electron.*, vol. 31, no. 5, pp. 3575–3585, May 2016.
[10] S. Selvakumar, M. Madhusmita, C. Koodalsamy, S. P. Simon, and Y. R. Sood, "High-speed maximum power point tracking module for PV systems," *IEEE Trans. Ind. Electron.*, vol. 66, no. 2, pp. 1119–1129, Feb. 2019.
[11] T. Esram and P. L. Chapman, "Comparison of photovoltaic array maximum power point tracking techniques," *IEEE Trans. Energy Convers.*, vol. 22, no. 2, pp. 439–449, Jun. 2007.
[12] D. Sera, L. Mathe, T. Kerekes, S. V. Spataru, and R. Teodorescu, "On the perturb-and-observe and incremental conductance MPPT methods for PV systems," *IEEE J. Photovolt.*, vol. 3, no. 3, pp. 1070–1078, Jul. 2013.
[13] A. K. Abdelsalam, A. M. Massoud, S. Ahmed, and P. N. Enjeti, "High-performance adaptive perturb and observe MPPT technique for photovoltaic-basedmicrogrids," *IEEE Trans. Power Electron.*, vol. 26, no. 4, pp. 1010–1021, Apr. 2011.
[14] N. Kumar, B. Singh, B. K. Panigrashi, and L. Xu, "Leaky-least-logarithmic-absolute-differencebased control algorithm and learning-based in C MPPT technique for grid-integrated PV system," *IEEE Trans. Ind. Electron.*, vol. 66, no. 11, pp. 9003–9012, Nov. 2019.
[15] D. Das, S. Madichetty, B. Singh, and S. Mishra, "Luenberger observer based current estimated boost converter for PV maximum power extraction—a current sensorless approach," *IEEE J. Photovolt.*, vol. 9, no. 1, pp. 278–286, Jan. 2019.
[16] Life Energy Motion (LEM). Datasheet: Current Transducer LTSR 6-NP. 2017. [Online]. Available: www.lem.com
[17] Allegro Microsystems., "Datasheet: ACS712 Fully integrated, hall-effect-based linear current sensor IC with 2.1 kVRMS isolation and a low-resistance current conductor," 2019. [Online]. Available: www.allegromicro.com
[18] A. Itzke, R. Weiss, and R. Wiegel, "Influence of the conductor position on a circular array of hall sensors for current measurement," *IEEE Trans. Ind. Electron.*, vol. 66, no. 1, pp. 580–585, Jan. 2019.

[19] Y. Chen, Q. Huang, and A. H. Khawaja, "An interference-rejection strategy for measurement of small current under strong interference with magnetic sensor array," *IEEE Sensors J.*, vol. 19, no. 2, pp. 692–700, Jan. 2019.

[20] B. George, Z. Tan, and S. Nihtianov, "Advances in capacitive, eddy current, and magnetic displacement sensors and corresponding interfaces," *IEEE Trans. Ind. Electron.*, vol. 64, no. 2, pp. 9595–9607, Dec. 2017.

[21] P. Midya, P. T. Krein, and M. F. Greuel, "Sensorless current mode control-an observer-based technique for dc-dc converters," *IEEE Trans. Power Electron.*, vol. 16, no. 4, pp. 522–526, Jul. 2001.

[22] N. Kasa, T. Iida, and L. Chen, "Flyback inverter controlled by sensorless current MPPT for photovoltaic power system," *IEEE Trans. Ind. Electron.*, vol. 52, no. 4, pp. 1145–1152, Aug. 2005.

[23] A. Chikh and A. Chandra, "An optimal maximum power point tracking algorithm for PV systems with climatic parameters estimation," *IEEE Trans. Sustain. Energy*, vol. 6, no. 2, pp. 644–652, Apr. 2015.

[24] M. Metry and R. S. Balog, "A model parity study on the model predictive control based sensorless current mode," in *Proc. IEEE Int. Conf. on Compatibility, Power Electron. and Power Eng*., Doha, Qatar, vol. 10–12 Apr. 2018, pp. 1–6.

[25] R. Min, Q. Tong, Q. Zhan, X. Zou, K. Yu, and Z. Liu, "Digital sensorless current mode control based on charge balance principle and dual current error compensation for dc–dc converters in DCM," *IEEE Trans. Ind. Electron.*, vol. 63, no. 1, pp. 155–165, Jan. 2016.

[26] M. Metry, M. Shadmand, R. S. Balog, and H. Abu-Rub, "MPPT of photovoltaic systems using sensorless current-based model predictive control," *IEEE Trans. Ind. Appl.*, vol. 53, no. 2, pp. 1157–1167, Mar./Apr. 2017.

[27] J. Hu, J. Zhu, G. Lei, G. Platt, and D. G. Dorrell, "Multi-objective model-predictive control for high-power converters," *IEEE Trans. Energy Convers.*, vol. 28, no. 3, pp. 652–663, 2013.

[28] Y. Lu, D. Li, Z. Xu, and Y. Xi, "Convergence analysis and digital implementation of a discrete-time neural network for model predictive control," *IEEE Trans. Ind. Electron*., vol. 61, no. 12, pp. 7035–7045, Apr. 2014.

[29] M. Metry, M. B. Shadmand, R. S. Balog, and H. Abu-Rub, "A variable step-size MPPT for sensorless current model predictive control for photovoltaic systems," *IEEE Energy Convers. Congr. Expo. (ECCE)*, Milwaukee, WI, vol. 18–22, Sep. 2016, vol. PP, pp. 1–8.

[30] M. B. Shadmand, S. Jain, and R. S. Balog, "Autotuning technique for the cost function weight factors in model predictive control for power electronic interfaces," *IEEE J. Emerg. Sel. Topics Power Electron.*, vol. 7, no. 2, pp. 1408–1420, Jun. 2019.

[31] H. T. Nguyen and J.-W. Jung, "Disturbance-rejection-based model predictive control: Flexible-mode design with a modulator for three-phase inverters," *IEEE Trans. Ind. Electron.*, vol. 65, no. 4, pp. 2893–2903, Apr. 2018.

[32] A. Kwasinski, W. Weaver, and R. S. Balog, *Microgrids and other Local Area Power and Energy Systems*. Cambridge, United Kingdom: Cambridge Univ. Press, 2016.

[33] S.-H. Lee, W.-J. Cha, B.-H. Kwon, and M. Kim, "Discrete-time repetitive control of flyback CCM inverter for PV power applications," *IEEE Trans. Ind. Electron*., vol. 63, no. 2, pp. 976–984, Feb. 2016.

[34] J. M. Guerrero, J. C. Vasquez, J. Matas, L. G. de Vicuna, and M. Castilla, "Hierarchical control of droop-controlled AC and DCmicrogrids—a general approach toward standardization," *IEEE Trans. Ind. Electron.*, vol. 58, no. 1, pp. 158–172, Jan. 2011.

[35] V. Pop, H. J. Bergveld, D. Danilov, P. P. L. Regtien, and P. H. L. Notten, *Battery Management Systems: Accurate State-of-Charge Indication for Battery-Powered Applications (Phillips Research)*. Dordrecht: Springer, 2008.

[36] S. Harb, M. Mirjafari, and R. S. Balog, "Ripple-port module-integrated inverter for grid-connected PV applications," *IEEE Trans. Ind. Appl.*, vol. 49, no. 6, pp. 2692–2698, May 2013.

[37] R. S. Balog, M. Metry, and M. B. Shadmand, "The load as a controllable energy asset in dc microgrids," in *DC Distribution Systems and Microgrids*, T. Dragicevic, P. Wheeler, and F. Blaabjerg, Eds. 1st ed.: IET Publisher, 2018, pp. 153–187.

[38] M. Metry, M. B. Shadmand, R. S. Balog, and H. Abu Rub, "High efficiency MPPT by model predictive control considering load disturbances for photovoltaic applications under dynamic weather condition," in *Proc. IEEE Ind. Electron. Conf. (IECON)*, Yokohama, Jpn., vol. 9–12. Nov. 2015, pp. 4092–4095.

[39] J. B. Rawlings and D. Q. Mayne, *Model Predictive Control: Theory and Design*, Santa Barbara, California: Nob Hill Publishing LLC, 2009.

[40] L. Cheng *et al.*, "Model predictive control for DC–DC boost converters with reduced-prediction horizon and constant switching frequency," *IEEE Trans. Power Electron.*, vol. 33, no. 10, pp. 9064–9075, Oct. 2018.

[41] N. Guler and E. Irmak, "A model predictive control-based hybrid MPPT method for boost converters," *Int. J. Electron.*, pp. 1362–3060, Mar. 2019.

[42] A. El Khateb, N. Abd Rahim, J. Selvaraj, and B. W. Williams, "DC-to-DC converter with low input current ripple for maximum photovoltaic power extraction," *IEEE Trans. Ind. Electron.*, vol. 62, no. 4, pp. 2246–2256, Apr. 2015.

[43] S. A. Larrinaga, M. A. R. Vidal, E. Oyarbide, and J. R. T. Apraiz, "Predictive control strategy for DC/AC converters based on direct power control," *IEEE Trans. Ind. Electron.*, vol. 54, no. 3, pp. 1261–1271, Jun. 2007.

[44] M. Tomlinson, H. d. T. Mouton, R. Kennel, and P. Stolze, "A fixed switching frequency scheme for finite-control-set model predictive control—concept and algorithm," *IEEE Trans. Ind. Electron.*, vol. 63, no. 12, pp. 7662–7670, Dec. 2016.

[45] P. E. Kakosimos, A. G. Kladas, and S. N. Manias, "Fast photovoltaic-system voltage- or current-oriented MPPT employing a predictive digital current-controlled converter," *IEEE Trans. Ind. Electron.*, vol. 60, no. 12, pp. 5673–5685, Dec. 2013.

[46] R. Bründlinger, N. Henze, H. Häberlin, B. Burger, A. Bergmann, and F. Baumgartner, "in *Proc. prEN 50530 - New Eur. Standard Perform. Characterisation PV Inverters,"* presented at 24th Europe Photovoltaic Solar Energy Conference, Germany, pp. 21–25. Sep. 2009.

[47] A. Andreas and S. Wilcox, "Observed atmospheric and solar information system (OASIS) - SOLRMAP university of arizona: 2018 Data," in *NREL Report No. DA-5500-56494*, ed. Tucson, Arizona (Data, 2010): [Online]. Available: http://dx.doi.org/10.5439/1052226

[48] M. A. Elgendy, B. Zahawi, and D. J. Atkinson, "Assessment of the incremental conductance maximum power point tracking algorithm," *IEEE Trans. Sustain. Energy*, vol. 4, no. 1, pp. 108–117, Jan. 2013.

[49] M. Metry and R. S. Balog, "A parameter mismatch study on model predictive control based sensorless current mode," in *IEEE Texas Power and Energy Conf. (TPEC)*, College Station, TX, vol. 8–9 Feb 2018, pp. 1–6.

[50] M. A. G. d. Brito, L. Galotto, L. P. Sampaio, G. d. A. e. Melo, and C. A. Canesin, "Evaluation of the main MPPT techniques for photovoltaic applications," *IEEE Trans. Ind. Electron.*, vol. 60, no. 3, pp. 1156–1167, Mar. 2013.

[51] C.-C. Hua, Y.-H. Fang, and W.-T. Chen, "Hybrid maximum power point tracking method with variable step size for photovoltaic systems," *IET Renewable Power Gener.*, vol. 10, no. 2, pp. 127–132, Feb. 2016.

[52] H. A. Sher, A. F. Murtaza, A. Noman, K. E. Addoweesh, K. Al-Haddad, and M. Chiaberge, "A new sensorless hybrid MPPT algorithm based on fractional short-circuit current measurement and P&O MPPT," *IEEE Trans. Sustain. Energy*, vol. 6, no. 4, pp. 1426–1434, Oct. 2015.

[53] Y. Levron and D. Shmilovitz, "Maximum power point tracking employing sliding mode control," *IEEE Trans. Circuits Syst. I: Regular Papers*, vol. 60, no. 3, pp. 724–732, Mar. 2013.

[54] A. M. Bazzi and P. T. Krein, "Ripple correlation control: An extremum seeking control perspective for real-time optimization," *IEEE Trans. Power Electron.*, vol. 29, no. 2, pp. 988–995, Feb. 2014.

[55] F. Paz and M. Ordonez, "High-performance solar MPPT using switching ripple identification based on a lock-in amplifier," *IEEE Trans. Ind. Electron.*, vol. 63, no. 6, pp. 3595–3604, Jun. 2016.

[56] "*Technical regulation 3.2.2 for PV power plants with a power output above 11 kW*," 14/17997-39 ed. Danish Grid Codes: energinet.dk, 2016.

[57] S. A. Arefifar, F. Paz, and M. Ordonez, "Improving solar power PV plants using multivariate design optimization," *IEEE J. Emerg. Sel. Topics Power Electron.*, vol. 5, no. 2, pp. 638–650, Jun. 2017.

[58] SMA Solar Technology AG, "Maximum freedom when oversizing: More flexibility and higher profitability for PV projects with sunny central inverters," in "*OVERSIZING WHITEPAPER*," [Online]. Available: https://www.sma.de/fileadmin/content/global/specials/documents/oversizing/Whitepaper_Oversizing_EN_180530_01.pdf

[59] H. D. Tafti *et al.*, "Extended functionalities of photovoltaic systems with flexible power point tracking: Recent advances," *IEEE Trans. Power Electron.*, vol. 35, no. 9, pp. 9342–9356, Sep. 2020.